Contents lists available at ScienceDirect

Applied Catalysis B: Environmental

Insights into the photosensitivity activity of BiOCl under visible light irradiation

Jinli Hu, Wenjie Fan, Weiqing Ye, Caijin Huang, Xiaoqing Qiu *

Research Institute of Photocatalysis, State Key Laboratory of Photocatalysis on Energy and Environment, College of Chemistry, Fuzhou University, Gongye Rd. 523, Fuzhou 350002, China

ARTICLE INFO

ABSTRACT

In-depth understanding the dye sensitization process over the semiconductor is the key issue for the applications of dye-sensitized solar cells, hydrogen production, and environmental remediation. This work addresses the role of high-quality BiOCl nanoplates in the photosensitization process. It is found that there exists a strong interaction between Rhodamine B and BiOCl nanoplates, which greatly improves the electronic conductivity for interfacial electron injection. The fluorescence emission of Rhodamine B is thus markedly suppressed by the addition of BiOCl suspension, resulting from the electron injection from excited Rhodamine B into the conduction band of BiOCl nanoplates. Moreover, benefitting from the proper conduction band edge potential of BiOCl nanoplates, the injected electrons can be trapped by the surface absorbed O_2 to generate reactive oxygen species, resulting in the high photosensitization activity for the Rhodamine B degradation under visible light irradiation.

1. Introduction

The sensitization of semiconductor via surface absorbed color dye molecules plays a vital role in activating visible light absorption in the field of photography, photovoltaic and photoelectrochemistry [1–4]. It is widely accepted that the sensitization can be achieved by the excitation of dye molecules under light irradiation and the subsequent electron transfer from the excited dye molecules into the conduction band of semiconductor [5,6]. Generally, effective sensitization depends on the choice of suitable dye, adsorption of dye molecules on the surfaces of semiconductor, and energy matching of the excited state of dye and the semiconductor conduction band edge [7,8]. With the aim to enhance the light energy conversion efficiency, much effort has been devoted to promoting the electron transfer during the sensitization process in dye-sensitized solar cells, mainly concentrating on the attachment of dye molecules on the semiconductor surface and light harvesting to improve the photocurrent [7,9], wherein the semiconductor is considered as an electron-transfer mediator [5]. As a matter of fact, the injected electrons from the excited dye molecules can be trapped by O_2 to generate reactive oxygen species due to the proper redox potential of the conduction band of semiconductor,

which are then subject to the detoxification of pollutants and/or water splitting [3,4]. Accordingly, the dye sensitization technique can also find its another important applications in hydrogen production [10,11], and environmental remediation [12–14], namely, the sensitized photocatalysis [3,4]. However, as suggested by Prof. Ohtani [15,16], the sensitization process causes difficulties in investigating the mechanism of the photocatalysis, especially for the semiconductor photocatalysts with visible light activities. Therefore, an in-depth understanding of dye sensitization processes that occur on the surface of semiconductors, including interaction of the dye and the semiconductor, electron injection, the formation of the reactive oxygen species, and the role of semiconductor, is still urgently required.

Bismuth based semiconductors have attracted intensive attention due to their promising applications as ferroelectric materials, selective oxidation catalysts, pigments, photocatalysts, and photoelectrodes for dye sensitized solar cells [17–21]. Among them, bismuth oxychloride (BiOCl) has a tetragonal layered structure consisting of [Cl—Bi—O—Bi—Cl] sheets together by the nonbonding interaction through the Cl atoms along the *c*-axis [22]. The strong internal static electric fields perpendicular to the Cl layer and the bismuth oxide-based fluorite-like layer endow the effective separation of the charge carriers [23]. Furthermore, BiOCl belongs to the family of wide indirect band-gap semiconductors with negligible photocatalytic properties under visible light irradiation [22], which can be considered as an ideal candidate for the study of sensitization

---

* Corresponding author. Tel.: +86 591 83969021; fax: +86 591 83969021.
E-mail address: qiuxq@fzu.edu.cn (X. Qiu).

process by excluding the self-photoabsorption of the semiconductor [15,16]. Recently, BiOCl nanostructures with a diversity of well-controlled morphologies have been successfully obtained using various methods, including nanobelts [24], nanofibers [25], nanoplates [26–28], nanosheets [29,30] and nanoflakes [28,31]. For instance, Zhang et al. prepared the BiOCl single-crystalline nanosheets with highly facet-dependent photoreactivity by a hydrothermal method [23]. Chen et al. reported that the square-like nanoplates showed excellent photocatalytic performance via photosensitization pathway under visible light illumination [32]. Wang et al. further demonstrated that the porous BiOCl micro flowers consisted of ultrathin nanosheets had superior photosensitization activities [33]. Despite the recent significant progress in the BiOCl photocatalysis and preparation [34–36], little is known about the nature of the sensitization processes over BiOCl. Herein, we prepared high quality BiOCl nanocrystals by a facile hydrothermal method without any surfactants. The photosensitization activities were explored by using the decomposition of Rhodamine B (RhB) as the probe. The electron injection process involving the semiconductor was investigated by fluorescence spectra and electrochemical impedance spectra. It is found that, compared with the most commonly used wide gap semiconductor (TiO_2, Degussa, P-25), our BiOCl samples exhibited an excellent photosensitization activity for RhB degradation, resulting from the strong adsorption of the RhB dye molecules over the surfaces, the effective electron injection, and the sequent reactive radicals formation.

2. Experimental

2.1. Preparation of BiOCl samples

The BiOCl samples were synthesized from mixed solvent of water and ethanol through a facile one-step hydrothermal process. In a typical procedure, 0.005 mol of $BiCl_3$ was added in a certain amount of ethanol (35, or 60 mL) at room temperature under stirring for 25 min, and 0.01 mol NaOH was dissolved into distilled water (30, or 5 mL). For the synthesis of BiOCl without ethanol, 0.005 mol of $BiCl_3$ was dispersed in 5 mL of distilled water, while 0.01 mol NaOH was dissolved into 60 mL of distilled water. Then, the clear NaOH solution was added into $BiCl_3$ to give a suspension with a total volume of 65 mL under stirring for 20 min. The mixture suspension was then transferred to a 100 mL Teflon-lined stainless steel autoclave. The autoclave was treated at 160 °C for 4 h, and air cooled to room temperature. The resulting samples were collected and washed with deionized water several times and dried at 70 °C in air.

2.2. Sample characterization

The powder X-ray diffraction (XRD) measurements were recorded on a Rigaku MinFlex II benchtop X-ray diffractometry with Cu-Ka irradiation. The ionic characteristics and surface composition were studied by X-ray photoelectron spectroscopy (XPS, Perkin-Elmer model 5600). The C1s signal was used to correct the charge effects. The morphologies and microstructures of the samples were investigated by field-emission scanning electron microscope (FESEM) using a Hitachi New Generation SU8010 apparatus and transition electron microscopy (TEM) on a Hitachi HF-2000 instrument under an acceleration voltage of 200 kV. Nitrogen adsorption measurements were carried out at 77 K using a 3020 system utilizing Brunauer–Emmett–Teller (BET) technique. UV–visible absorption spectra were obtained by the diffuse reflection method using a Lambda 950 UV/vis spectrophotometer. Fluorescence emission spectra of RhB solution were recorded on an Edinburgh FL/FS900 spectrophotometer at room temperature.

Raman scattering measurements were performed with a multichannel modular triple Raman system (Renishaw Co.) with confocal microscope at room temperature using the 532 nm laser.

2.3. Photosensitization activity test

RhB, a common xanthene dye, was used as a probe molecule to evaluate the photosensitization reactivity of BiOCl under visible light irradiation. The photosensitization experiments were performed at ambient temperature using a 150 W Xe lamp with a 420 nm cutoff filter as visible light source. Typically, 0.01 g of our sample was added into 50 mL of 10 mg/L RhB aqueous solution in a container. Prior to irradiation, the suspension was stirred under dark for 4 h to ensure the establishment of adsorption/desorption equilibrium. During the irradiation, the suspension was kept continuously stirring with a magnetic stirrer. At given intervals, certain amount of the suspension was extracted and subsequently centrifuged. The concentration of RhB in the supernatant was monitored by the UV–visible absorption spectra measured with a Cary-50 UV–visible spectrometer.

2.4. Photoelectrochemical measurements

Fluorine-doped tin oxide (FTO) substrates were thoroughly rinsed ultrasonically with acetone, isopropanol, and ethanol. The edges of the FTO substrates were covered with adhesive tape. 5 mg of our samples was dispersed in 800 uL dimethylformamide under sonication for 1 h to produce slurry. The as-obtained slurry was spread onto the conductive surface of the FTO glass to form a film with an area of 0.25 cm^2. Subsequently, the uncovered parts of the FTO glass were isolated with epoxy resin.

The flat-band potential of the sample was carried out by a conventional three-electrode electrochemical cell. The as-obtained FTO film was used as the working electrode, a platinum electrode was used as the counter electrode, and reference electrode was Ag/AgCl. All the electrodes were immersed in a sodium sulfate electrolyte solution (0.2 M). Electrochemical impedance spectroscopy (EIS) experiments were measured on a Zennium electrochemical workstation (Zahner, Germany). EIS investigation was carried out under AC polarization with a frequency range from 4 to 100 MHz at the DC open circuit potential (OCP). The flat-band potentials of the semiconductors were electrochemically determined from the Mott–Schottky plots.

3. Results and discussions

Fig. 1 gives the XRD patterns of the BiOCl samples obtained at 160 °C for 4 h from the mixed solvent with different amount of ethanol. As can be seen, the diffraction peaks of the samples can be easily indexed to a pure tetragonal matlockite BiOCl phase, which are in good consistence with the reference data (JCPS card No. 6-249). No other phase peaks of impurities associated with the narrow band gap Bi_2O_3 [37] are observed, suggesting the high purity of the as-obtained samples. In addition, it can be observed that the peak intensities of (0 0 1) facets family, such as (0 0 1), (0 0 2) and (0 0 3) become weaker as the ethanol amount increasing in the synthesis condition, compared with the peaks of (1 0 1), (1 1 0) and (1 0 2), implying the crystal panel direction of the obtained samples can be slight controlled by tuning the ethanol amount in the mixed solvent.

The morphologies and microstructures of the samples were investigated by SEM and TEM observations. Typical SEM images of the BiOCl samples obtained from the mixed solvent with different ethanol amounts are shown in Fig. 2. It is clear that all the BiOCl samples are in the shape of nanoplates with well-defined edges and smooth surfaces. The amount of ethanol in the mixed solvent has an
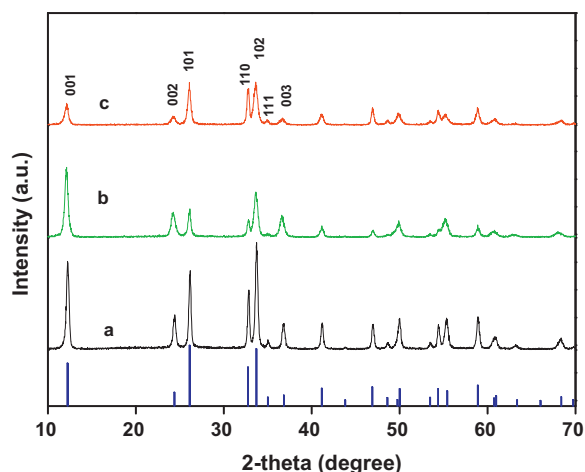
Fig. 1. XRD patterns of BiOCl samples obtained from the mixed solvent with various amount of ethanol. (a) without ethanol, (b) 35 mL of ethanol, (c) 60 mL of ethanol. Vertical bars below the patterns represent the standard diffraction data from JCPDS file for bulk BiOCl (No. 6-249).

obvious impact on the particle size and size distribution. The BiOCl nanoplates obtained from the solvent without ethanol display a relatively broad size distribution and the biggest nanoplate is larger than 1 μm in the lateral size (Fig. 2a). Interestingly, the particle size and distribution reduced as increasing the ethanol amount in the mixed content (Fig. 2b and c). Uniform BiOCl nanoplates with a narrow particle distribution were obtained as the amount of ethanol increase to 60 mL (Fig. 2c). It is well known that BiCl₃ is susceptible to hydrolysis in water to form bulk BiOCl compound [38]. Due to that ethanol can effectively decrease the hydrolysis process [31], the growth rate of BiOCl should be slowed down in the mixed solvent as the amount ethanol increasing, which benefits the formation of uniform BiOCl nanoplates. A low-magnification TEM

image (Fig. 2d) further shows the typical plate-like nanocrystals of the BiOCl sample obtained from the mixed solvent with 60 mL ethanol, which is consistent with the analytical results based on the SEM observations. A lattice-resolved HRTEM image taken from the edge of the nanoplate shows the lattice fringes of 0.273 nm, corresponding to the interplanar spacing of the (1 1 0) of BiOCl, demonstrating the single-crystal nature of the BiOCl nanoplates. Moreover, the fast-Fourier transform (FFT) pattern clearly shows the (1 1 0), (2 0 0) and (1 -1 0) planes and the set of diffraction spots can be indexed as the (0 0 1) zone axis of tetragonal BiOCl.

XPS was employed to further investigate the chemical states of surface elements of the as-prepared BiOCl samples. The binding energy values were calibrated with the C 1s signal at 284.6 eV. The survey spectrum (Fig. 3a) shows only the C, Bi, O and Cl signals at the surface. The presence of carbon mainly comes from the hydrocarbon of the XPS instrument itself. The O 1s core level spectrum gives a sharp peak at 529.9 eV, which belongs to O^{2-} from the Bi—O bond in BiOCl (Fig. 3b). As displayed in Fig. 3c, two well resolved peaks located at 159.3 and 164.6 eV are observed in the Bi 4f core level spectrum, which are in good agreement with the characteristic of Bi^{3+} in the BiOCl [39,40]. No shoulders associated with Bi^{2+}, Bi^{4+} or Bi^{5+} state in bismuth oxides was observed, indicating the high purity of our samples [40,41]. Additionally, as shown in Fig. 3d, the Cl 2p core level spectrum is resolved into two peaks at 198.0 and 199.6 eV, which are assigned to Cl $2p_{3/2}$ and Cl $2p_{1/2}$ region for BiOCl, respectively [25]. In order to probe the structural and vibrational features of BiOCl samples, the Raman spectra were next performed in the range of 50–600 cm^{-1}. As depicted in Fig. 4, all the three BiOCl samples show similar Raman spectra, which consist of three remarkable bands at approximately 59, 145, and 200 cm^{-1}, as well as one weak band at about 400 cm^{-1}. The strongest band located at 145 cm^{-1} can be assigned to the A_{1g} internal Bi—Cl stretching mode, while the band at 59 cm^{-1} also comes from the A_{1g} internal Bi—Cl stretching mode [42]. The band of 200 cm^{-1} is attributed to the E_g internal Bi—Cl stretching mode. Moreover, the weak and readily unnoticeable band at about
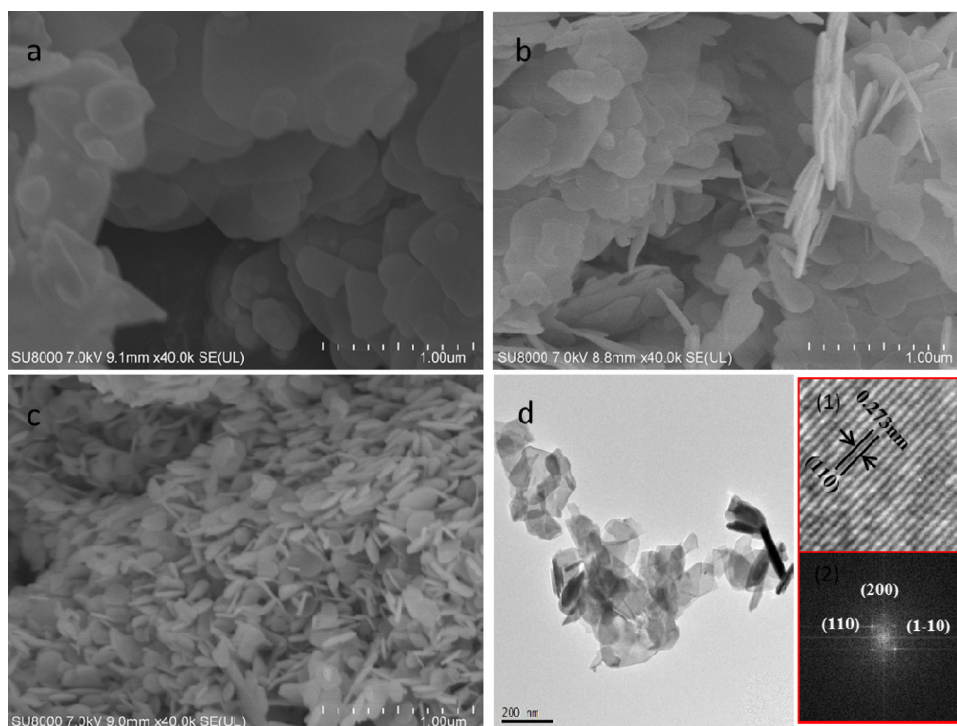

Fig. 2. SEM images of BiOCl samples obtained from the mixed solvent with various amount of ethanol. (a) without ethanol, (b) 35 mL of ethanol, (c) 60 mL of ethanol. (d)TEM image of (c), Inset: the corresponding HRTEM images ant the FFT patterns.
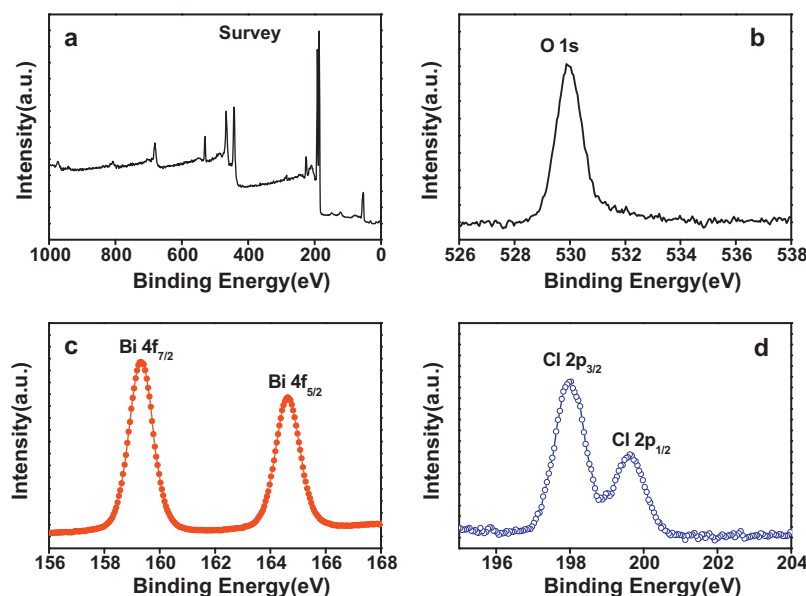
Fig. 3. XPS spectra of BiOCl samples. (a) survey XPS spectrum, (b) O 1s core-level spectrum, (c) Bi 4f core-level spectrum, (d) Cl 2p core-level spectrum.

$400 \, cm^{-1}$ should origin from the E_g and B_{1g} modes produced by the motion of the oxygen atoms. These Raman data analyses are in good agreement with the literature reports [32,42], thus confirming that the high quality of the BiOCl samples were obtained by our synthesis method.

Optical absorption properties of the semiconductor materials play a significant role in the photosensitization activity. Thus, the UV–visible absorption spectra of the samples were measured by diffuse reflectance spectroscopy (DRS) at room temperature, which are illustrated in Fig. 5. The spectrum of P-25 is also presented for comparison. It is seen that the BiOCl samples are transparent in the visible region, ruling out the photoabsorption of our samples in the following photosensitization study. All the BiOCl samples show intense absorption edges in the UV region at about 370 nm, which is characteristic absorption behavior of the wide-band-gap semiconducting oxide. It is well known that the optical absorption of a crystalline semiconductor near the band edge follows the formula $(\alpha h v) = A(h v - E_g)^n$, where α, v, E_g, and A are the absorption coefficient, light frequency, band gap energy, and a constant, respectively [13,43]. The value of n depends on the characteristics of the transition of the semiconductor. The value of n for

BiOCl is 2 because it belongs to the indirect semiconductor [22]. By extrapolating the straight portion of $(\alpha h v)^{1/2}$ versus plot to $(\alpha h v)^{1/2} = 0$ (inset of Fig. 5), The E_g of BiOCl samples was determined to be 3.4 eV, a value that is close to the reported ones [22]. The optical properties of the sample are expected to simplify the role of semiconductor in the photosensitization process.

The photosensitization activities of the as-obtained samples were next studied through the degradation of RhB under visible light ($\lambda \geq 420$ nm) irradiation at room temperature. Fig. 6a shows the typical evolution of absorption spectra of RhB dye aqueous solution over BiOCl samples during the visible light irradiation. The photographs in insets of Fig. 6a illustrate that the color of the dye solution faded as the exposure time increasing. Accompanying the diminishment of the RhB characteristic absorption peaks at 553 nm, the absorption peaks in the range of 200–300 nm gradually decline with extending the exposure time, suggesting the destruction of the conjugated structure of RhB. No new absorption bands and negligible hypsochromic shift is observed, implying that the absence of *N*-de-ethylation of RhB [44]. Complete degradation of the RhB dye was achieved after 12 min over the BiOCl nanoplates obtained from
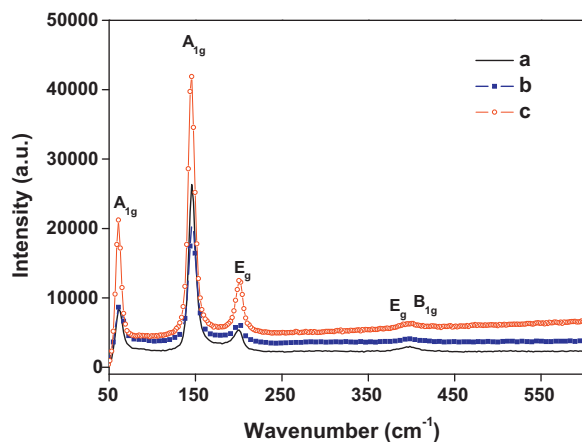

Fig. 4. Raman spectra of BiOCl samples obtained from the mixed solvent with various amount of ethanol. (a) without ethanol, (b) 35 mL of ethanol, (c) 60 mL of ethanol.
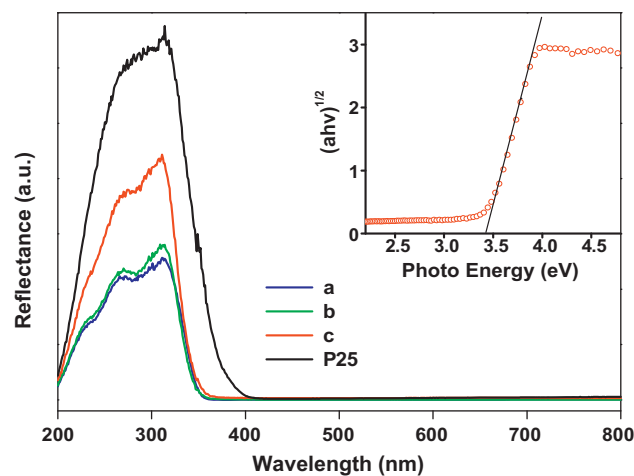

Fig. 5. UV–visible spectra of P-25 and BiOCl samples obtained from the mixed solvent with various amount of ethanol. (a) without ethanol, (b) 35 mL of ethanol, (c) 60 mL of ethanol. Inset: Plots of $(\alpha h v)^{1/2}$ vs photon energy of BiOCl samples.
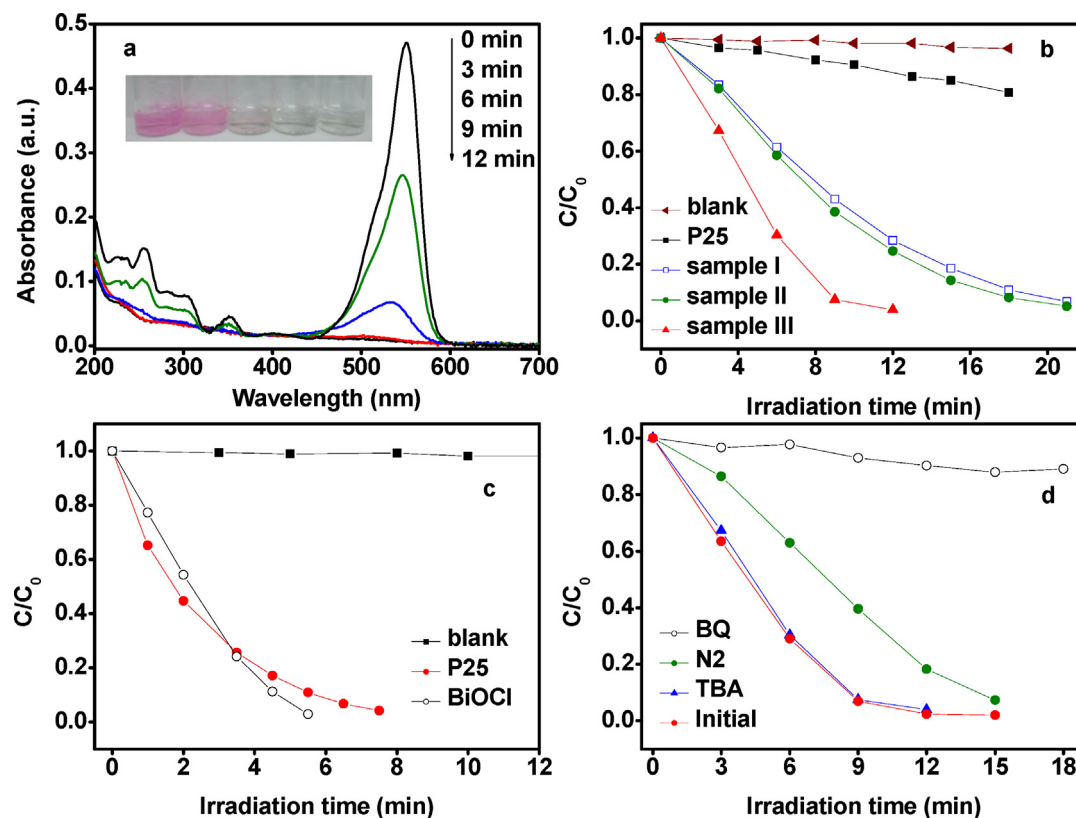
Fig. 6. (a) The temporal evolution of the absorption spectra of RhB over BiOCl samples obtained from the mixed solvent with 60 mL of ethanol under visible light irradiation, inset: the photographs of the dye solution during the irradiation process, (b) Comparative studies of RhB degradation under visible light irradiation over P-25 and BiOCl samples obtained with various amount ethanol, (Sample I) without ethanol, (Sample II) 35 mL of ethanol, (Sample III) 60 mL of ethanol. (c) Degradation of RhB over P-25 and BiOCl nanoplates obtained from mixed solvent with 60 mL of ethanol under irradiation with UV light. (d) Active species capture experiments over BiOCl nanoplates under visible light irradiation.

the mixed solvent with 60 mL ethanol. Comparative studies on the degradation of RhB dye over all the BiOCl samples and commercial P-25 were further performed under the same condition. As shown in Fig. 6b, all the BiOCl samples show excellent activities for the RhB degradation, wherein the BiOCl nanoplates obtained from the mixed solvent with 60 mL ethanol exhibit the best performance. Surprisingly, the most commonly used wide gap semiconductor (P-25) shows very limited activity for the RhB degradation under the identical condition. To verify the quality of the used P-25 and specify the difference between the BiOCl and TiO$_2$, we conducted the photogradation experiments under the irradiation of Xenon lamp without cut-off filters, namely, the irradiation containing UV light. As shown in Fig. 6c, both BiOCl nanoplates and P-25 exhibit high activities for the RhB degradation, demonstrating that both materials can act as good photocatalysts. These experimental results reveal that BiOCl nanoplates possess high performance for the RhB degradation both under visible light and UV light irradiation, while P-25 only represents the UV light activity. In order to explore the reaction mechanism of the degradation of RhB over BiOCl nanoplates under visible light irradiation, the effects of various radical scavengers are studied. As shown in Fig. 6d, compared with the initial data, the degradation of RhB remains unchanged after the addition of *tert*-butyl alcohol (TBA, •OH radical scavenge), suggesting that •OH was not the main reactive radicals [26]. However, the introduction of benzoquinone (BQ, O^{2-}•radical scavenge) [45] leads to a marked suppression of the degradation rate of RhB, suggesting that O^{2-}•radical is primarily responsible for the degradation. Moreover, if the experiment was performed with purging nitrogen to remove the dissolved oxygen in the solution, the degradation of RhB was also evidently inhibited, further confirming that

O$_2$ plays a significant role in the sensitization degradation of dyes by BiOCl under visible light. As discussed above, the BiOCl nanoplates do not give the self-photoabsorption under the visible light irradiation due to its wide gap band. Therefore, it can be deduced that the adsorbed RhB dye molecules were excited to generate excited state RhB* that donated the electrons to the conduction band of BiOCl. Subsequently, the electrons injected were captured by the oxygen molecules adsorbed on the surface of BiOCl, which then generated the reactive radical O^{2-}•for the degradation of RhB dye [33].

Indeed, the effective electron injection and the subsequent formation of O^{2-}•radicals require the good energy matching and enough redox potential of the conduction band of semiconductor [5,46]. In general, the conduction band potential of *n*-type semiconductor is very close to the flat-band potential (V_{fb}) [47]. Thus, we measured the V_{fb} of the BiOCl samples and P-25 by an electrochemical method. Typical Mott–Schottky plots in the dark for BiOCl and P-25 are presented in Fig. 7a and b, which indicated the BiOCl and P-25 semiconductors belong to *n*-type due to the positive slop of the linear plot [48,49]. The V_{fb} value of BiOCl is determined to be about −1.3 V versus Ag/AgCl at pH = 7 (equivalent to −1.1 V vs. normal hydrogen electrode (NHE) at pH = 7), while the V_{fb} value of P-25 is about −0.49 V vs. NHE. Based on the above DRS measurements, we can figure out the valence band potentials are 2.22 and 2.71 V for BiOCl and P-25, respectively. It seems that both BiOCl and P-25 have the sufficient potentials of the conduction band and valence band edges for the mineralization of almost all organic contaminants, which accounts for their high performances under UV light irradiation. Furthermore, it is reported that the redox potentials of RhB and RhB* are 0.95 and −1.42 V vs NHE, respectively [14,50]. As illustrated in Fig. 7c, the energy level of the excited RhB* is located
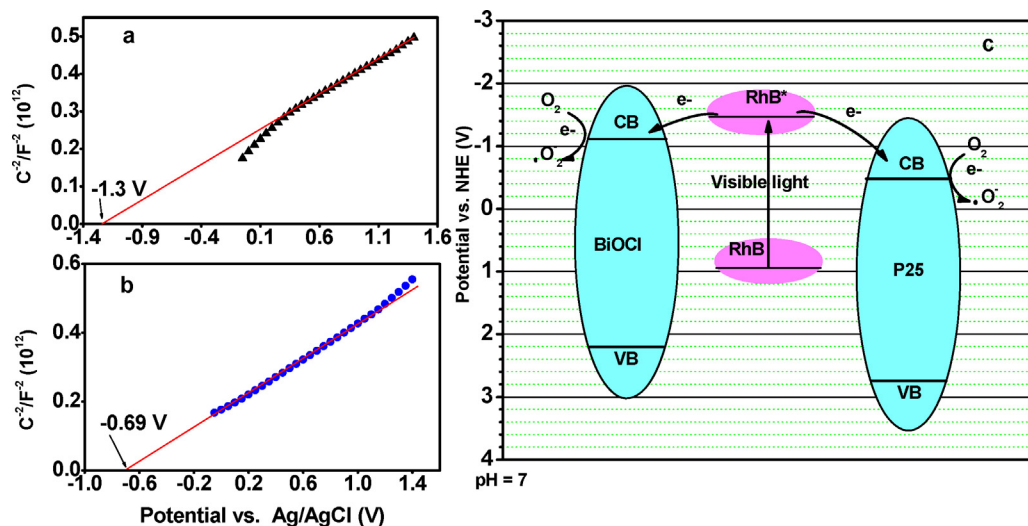
Fig. 7. Mott–Schottky plot for BiOCl (a) and P-25 (b) in 0.2 M Na$_2$SO$_4$ aqueous solution (pH = 7), (c) The energy diagram of RhB, BiOCl, and P-25.
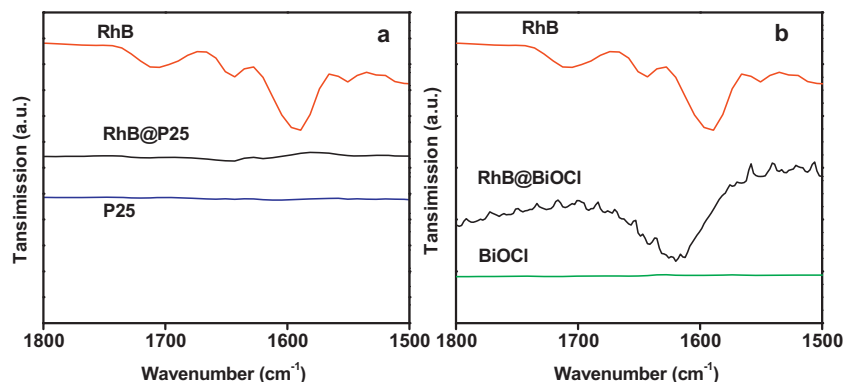

Fig. 8. (a) FTIR spectra of (a) P-25, RhB @P-25, and RhB. (b) FTIR spectra of BiOCl, RhB@BiOCl, and RhB.

well above the bounds of the conduction band of both BiOCl and P-25, providing a favorable driving force for the electron injection. On the other hand, the injected electrons in the conduction band can react with oxygen molecules to form reactive radicals because of their negative conduction band edge potentials of both BiOCl and P-25 [51]. This analysis explains the degradation of RhB dye over BiOCl nanoplates under visible light irradiation, and also raises interesting fundamental questions about the huge difference in the photosensitization activities between BiOCl and P-25, in spite of their similar electronic band structures.

To elucidate the factors behind the high photosensitivity of BiOCl nanplates, the adsorption behavior of the RhB dye was investigated, since the effective adsorption of dye molecules at the semiconductor surfaces is the essential requirement for the sensitization process [9]. The BET specific surface area of the BiOCl nanoplates is 16 m^2/g, and that of P-25 is about 50 m^2/g calculated from the from N$_2$ isotherms at 77 K. After stirring 4 h under dark at 25 °C, the adsorption amounts of RhB were determined to be 59% and 52% over BiOCl nanoplates and P-25, respectively. That is, the adsorption capability of P-25 is compatible with that of BiOCl nanoplates. Moreover, the absorption modes of RhB over P-25 and BiOCl were detected by FTIR measurements. As shown in Fig. 8a, it is very hard to observe the any vibration bands associated with RhB molecules for P-25 after the treatment of RhB solution for 4 h under dark, indicating that the RhB dye is probably simply attached on the P-25 surfaces by physisorption, which can be easily removed with water rinsing. Interestingly, an additional band

located at 1619 cm^{-1} is clearly observed for the RhB treated BiOCl nanoplates (Fig. 8b). This new vibration band can be ascribed to the interaction between —N—Et^{2+} group of BhB and O$^-_{surface}$ of BiOCl [52,53], demonstrating the existence of chemisorption over BiOCl [33]. Such strong adsorption is expected to facilitate the electron injection from the excited RhB into the conduction band of BiOCl nanoplates. Therefore, the photosensitized electron injection was further studied by using the fluorescence emission spectra of RhB
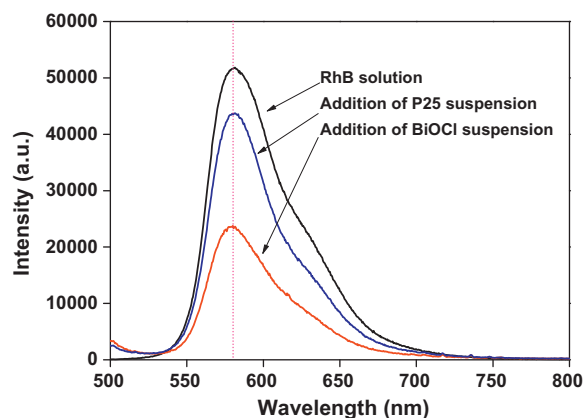

Fig. 9. The effects of the introduction BiOCl and P-25 colloidal suspension on the fluorescence emission spectra of RhB.
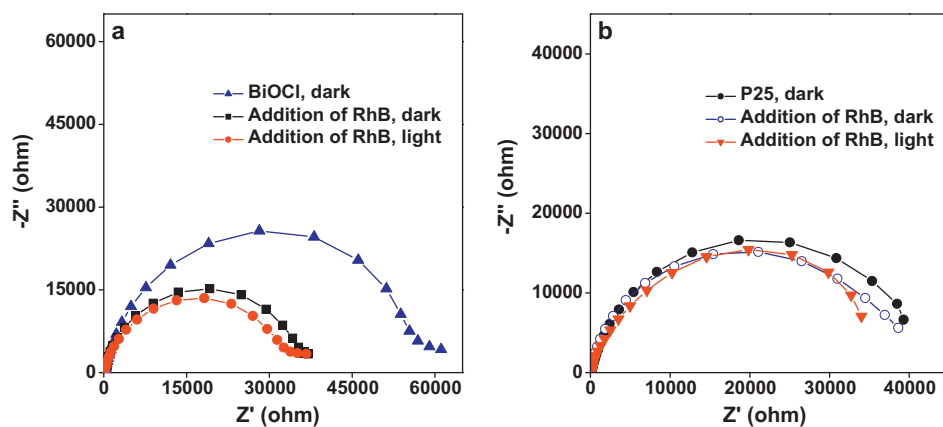
Fig. 10. The effects of introduction of RhB dye and visible light irradiation on the Nyquist impedance plots. (a) BiOCl, (b) P-25.

dye solution as the probe [7]. As shown in Fig. 9, the RhB solution has a strong fluorescence emission at 580 nm (excited at 532 nm). After the addition of P-25 colloidal suspension, the intensity of the fluorescence decrease, mainly due to the concentration quenching effect [7], since some RhB molecules could be adsorbed on the P-25 surfaces. As BiOCl nanoplates colloidal suspension (the amount equal to that of P-25) was added into the RhB solution, it can be seen that the fluorescence emission was remarkably decreased. Considering the similar adsorption capabilities of P-25 and BiOCl, the fluorescence quenching confirms that the electron transfer from the excited RhB dye to the BiOCl nanoplates is much more effective than P-25 [7,54]. To get the deeper insights into the electron injection process, the effects of RhB dye and light irradiation on the electrochemical impedance spectra (EIS) of the BiOCl and P-25 films were explored. As shown in Fig. 10, all Nyquist plots contain a macro arc part corresponding to interfacial electron charges transfer resistance [55]. The radium of the BiOCl nanoplates film is rather large under dark, indicating its big resistance. Encouragingly, upon the introduction of RhB dye into the electrolyte solution, the semicircle arc reduces even under dark, suggestion the adsorption of RhB can decrease resistance of the BiOCl electrode due to their strong interaction. The electronic conductivity of the BiOCl electrode can be further increase under visible light irradiation, further evidencing the electron injection from the dye into the electrode. However, it is worth noting that the negligible improvement of the electronic conductivity of P-25 electrode was achieved by the introduction of RhB dye and visible light irradiation (Fig. 10b). All these results unambiguously reveal that the origins of the high photosensitization activity of the BiOCl nanoplates comes from the strong adsorption of the dye molecules over the surfaces, the effective electron injection, and the sequent reactive radicals formation due to its suitable conduction band edge potential.

4. Conclusions

In summary, high-quality BiOCl nanoplates were synthesized via a facile one-step hydrothermal method from the mixed solvent of water and ethanol. Inspite of its wide band gap of 3.4 eV, the as-obtained BiOCl nanoplates exhibit excellent activity for the degradation of RhB dye solution under visible light irradiation. It is found that the degradation was undergone through a photosensitization pathway, in which the $O^{2-}\cdot$ specials are the main reactive radicals. The strong interaction of the absorbed dye molecules over the surfaces can effectively reduce the interfacial electron charges transfer resistance, facilitating the injection of the electrons from the excited dyes into the conduction band of BiOCl, which were trapped by semiconductor surface absorbed O_2 to generate reactive

oxygen species, resulting in the high photosensitization activity. This finding provides us good understanding for the role of the semiconductor in the sensitization process.

Acknowledgments

References

[1] M. Grätzel, Nature 414 (2001) 338–344.
[2] B. O'regan, M. Grfitzeli, Nature 353 (1991) 24.
[3] P.V. Kamat, Chem. Rev. 93 (1993) 267–300.
[4] A.L. Linsebigler, G. Lu, J.T. Yates Jr., Chem. Rev. 95 (1995) 735–758.
[5] P.V. Kamat, J. Phys. Chem. 93 (1989) 859–864.
[6] P. Persson, M.J. Lundqvist, R. Ernstorfer, W. Goddard, F. Willig, J. Chem. Theory Comput. 2 (2006) 441–451.
[7] J. Moser, M. Graetzel, J. Am. Chem. Soc. 106 (1984) 6557–6564.
[8] J.M. Rehm, G.L. McLendon, Y. Nagasawa, K. Yoshihara, J. Moser, M. Grätzel, J. Phys. Chem. 100 (1996) 9577–9578.
[9] K. Sayama, S. Tsukagoshi, K. Hara, Y. Ohga, A. Shinpou, Y. Abe, S. Suga, H. Arakawa, J. Phys. Chem. B 106 (2002) 1363–1371.
[10] T. Puangpetch, P. Sommakettarin, S. Chavadej, T. Sreethawong, Int. J. Hydrogen Energy 35 (2010) 12428–12442.
[11] Z. Jin, X. Zhang, Y. Li, S. Li, G. Lu, Catal. Commun. 8 (2007) 1267–1273.
[12] R.A. Larson, P.L. Stackhouse, T.O. Crowley, Environ. Sci. Technol. 26 (1992) 1792–1798.
[13] X. Qiu, G. Li, X. Sun, L. Li, X. Fu, Nanotechnology 19 (2008) 215703.
[14] Z. Xiong, L.L. Zhang, J. Ma, X. Zhao, Chem. Commun. 46 (2010) 6099–6101.
[15] X. Yan, T. Ohno, K. Nishijima, R. Abe, B. Ohtani, Chem. Phys. Lett. 429 (2006) 606–610.
[16] B. Ohtani, Chem. Lett. 37 (2008) 216–229.
[17] M. Francesconi, A. Kirbyshire, C. Greaves, O. Richard, G. Van Tendeloo, Chem. Mater. 10 (1998) 626–632.
[18] J. Hu, H. Li, C. Huang, M. Liu, X. Qiu, Appl. Catal., B: Environ. 142–143 (2013) 598–603.
[19] H. Yu, R. Liu, X. Wang, P. Wang, J. Yu, Appl. Catal., B: Environ. 111 (2012) 326–333.
[20] A. Luz, J. Conradt, M. Wolff, H. Kalt, C. Feldmann, Solid State Sci. 19 (2013) 172–177.
[21] L. Zhang, W. Wang, L. Zhou, M. Shang, S. Sun, Appl. Catal., B: Environ. 90 (2009) 458–462.
[22] K.-L. Zhang, C.-M. Liu, F.-Q. Huang, C. Zheng, W.-D. Wang, Appl. Catal., B: Environ. 68 (2006) 125–129.
[23] J. Jiang, K. Zhao, X. Xiao, L. Zhang, J. Am. Chem. Soc. 134 (2012) 4473–4476.
[24] H. Deng, J. Wang, Q. Peng, X. Wang, Y. Li, Chem. Eur. J. 11 (2005) 6519–6524.
[25] C. Wang, C. Shao, Y. Liu, L. Zhang, Scr. Mater. 59 (2008) 332–335.
[26] Y. Xie, F. Chang, C. Li, J. Chen, J. Luo, L. Li, X. Hu, CLEAN-Soil, Air, Water (2013).
[27] Z. Deng, D. Chen, B. Peng, F. Tang, Cryst. Growth Des. 8 (2008) 2995–3003.
[28] J. Ma, X. Liu, J. Lian, X. Duan, W. Zheng, Cryst. Growth Des. 10 (2010) 2522–2527.

[29] J. Geng, W.-H. Hou, Y.-N. Lv, J.-J. Zhu, H.-Y. Chen, Inorg. Chem. 44 (2005) 8503–8509.
[30] L. Ye, L. Zan, L. Tian, T. Peng, J. Zhang, Chem. Commun. 47 (2011) 6951–6953.
[31] Y. Li, J. Liu, J. Jiang, J. Yu, Dalton Trans. 40 (2011) 6632–6634.
[32] J. Xiong, G. Cheng, G. Li, F. Qin, R. Chen, RSC Adv. 1 (2011) 1542–1553.
[33] D.-H. Wang, G.-Q. Gao, Y.-W. Zhang, L.-S. Zhou, A.-W. Xu, W. Chen, Nanoscale 4 (2012) 7780–7785.
[34] Q. Mu, Q. Zhang, H. Wang, Y. Li, J. Mater. Chem. 22 (2012) 16851–16857.
[35] J. Xiong, G. Cheng, F. Qin, R. Wang, H. Sun, R. Chen, Chem. Eng. J. 220 (2013) 228–236.
[36] S. Weng, Z. Pei, Z. Zheng, J. Hu, P. Liu, ACS Appl. Mater. Interfaces 5 (2013) 12380–12386.
[37] L. Zhou, W. Wang, H. Xu, S. Sun, M. Shang, Chem. Eur. J. 15 (2009) 1776–1782.
[38] A. Wosylus, S. Hoffmann, M. Schmidt, M. Ruck, Eur. J. Inorg. Chem. 2010 (2010) 1469–1471.
[39] H.-Y. Jiang, K. Cheng, J. Lin, Phys. Chem. Chem. Phys. 14 (2012) 12114–12121.
[40] L. Ye, K. Deng, F. Xu, L. Tian, T. Peng, L. Zan, Phys. Chem. Chem. Phys. 14 (2012) 82–85.
[41] Y. Yu, C. Cao, H. Liu, P. Li, F. Wei, Y. Jiang, W. Song, J. Mater. Chem. A 2 (2014) 1677–1681.
[42] K. Zhang, J. Liang, S. Wang, J. Liu, K. Ren, X. Zheng, H. Luo, Y. Peng, X. Zou, X. Bo, Cryst. Growth Des. 12 (2012) 793–803.
[43] L. Zhang, W. Wang, L. Zhou, H. Xu, Small 3 (2007) 1618–1625.
[44] T. Watanabe, T. Takizawa, K. Honda, J. Phys. Chem. 81 (1977) 1845–1851.
[45] T.B. Li, G. Chen, C. Zhou, Z.Y. Shen, R.C. Jin, J.X. Sun, Dalton Trans. 40 (2011) 6751–6758.
[46] X. Qiu, M. Miyauchi, H. Yu, H. Irie, K. Hashimoto, J. Am. Chem. Soc. 132 (2010) 15259–15267.
[47] S.R. Morrison, Electrochemistry at Semiconductor and Oxidized Metal Electrodes, Plenum Press, New York, 1980, Chapter 4.
[48] S.Y. Chai, Y.J. Kim, M.H. Jung, A.K. Chakraborty, D. Jung, W.I. Lee, J. Catal. 262 (2009) 144–149.
[49] S. Weng, B. Chen, L. Xie, Z. Zheng, P. Liu, J. Mater. Chem. A 1 (2013) 3068–3075.
[50] T. Shen, Z.-G. Zhao, Q. Yu, H.-J. Xu, J. Photochem. Photobiol., A: Chem. 47 (1989) 203–212.
[51] X. Qiu, M. Miyauchi, K. Sunada, M. Minoshima, M. Liu, Y. Lu, D. Li, Y. Shimodaira, Y. Hosogi, Y. Kuroda, ACS Nano 6 (2012) 1609–1618.
[52] Q. Wang, C. Chen, D. Zhao, W. Ma, J. Zhao, Langmuir 24 (2008) 7338–7345.
[53] L. Pan, J.-J. Zou, X. Zhang, L. Wang, J. Am. Chem. Soc. 133 (2011) 10000–10002.
[54] K. Hashimoto, M. Hiramoto, T. Sakata, Chem. Phys. Lett. 148 (1988) 215–220.
[55] W. Yang, B. Ma, W. Wang, Y. Wen, D. Zeng, B. Shan, Phys. Chem. Chem. Phys. 15 (2013) 19387–19394.